

SPATIAL MODELING OF THE 3D MORPHOLOGY OF HYBRID POLYMER-ZNO SOLAR CELLS, BASED ON ELECTRON TOMOGRAPHY DATA¹

BY O. STENZEL, H. HASSFELD, R. THIEDMANN, L. J. A. KOSTER,
S. D. OOSTERHOUT, S. S. VAN BAVEL, M. M. WIENK, J. LOOS,
R. A. J. JANSSEN AND V. SCHMIDT

*Ulm University, Ulm University, Ulm University, Eindhoven University of
Technology, Eindhoven University of Technology, Eindhoven University of
Technology, Eindhoven University of Technology, Eindhoven University of
Technology, Eindhoven University of Technology and Ulm University*

A spatial stochastic model is developed which describes the 3D nanomorphology of composite materials, being blends of two different (organic and inorganic) solid phases. Such materials are used, for example, in photoactive layers of hybrid polymer zinc oxide solar cells. The model is based on ideas from stochastic geometry and spatial statistics. Its parameters are fitted to image data gained by electron tomography (ET), where adaptive thresholding and stochastic segmentation have been used to represent morphological features of the considered ET data by unions of overlapping spheres. Their midpoints are modeled by a stack of 2D point processes with a suitably chosen correlation structure, whereas a moving-average procedure is used to add the radii of spheres. The model is validated by comparing physically relevant characteristics of real and simulated data, like the efficiency of exciton quenching, which is important for the generation of charges and their transport toward the electrodes.

1. Introduction. Using methods from stochastic geometry and spatial statistics, a stochastic model is developed which describes the 3D nanomorphology of composite materials, being blends of two different (organic and inorganic) solid phases. Such materials are used, for example, in photoactive layers of hybrid polymer zinc oxide (ZnO) solar cells where the two solid phases play the role of a polymeric electron donor, consisting of, for example, poly(3-hexylthiophene), and an inorganic ZnO-electron acceptor, respectively. There is a great advantage of polymer solar cells due to their potentially low production costs, in comparison with classical silicon solar cells. However, the efficiency of polymer solar cells critically depends on the intimacy of mixing of the donor and acceptor semiconductors used

Received August 2010; revised March 2011.

¹Supported by Deutsche Forschungsgemeinschaft (DFG) under the Priority Programme: “Elementary Processes of Organic Photovoltaics” (SPP 1355).

Key words and phrases. Marked point process, parameter estimation, spatial statistics, stochastic geometry, adaptive thresholding, segmentation, model fitting, simulation, model validation, exciton quenching, polymer solar cells.

in these devices to create charges as well as on the presence of unhindered percolation pathways in the individual solid phases of the composite material to transport positive and negative charges toward electrodes; see, for example, [Yang and Loos \(2007\)](#). It is therefore very important to have tools at one's disposal which are suitable to analyze and model the 3D morphology of these materials quantitatively. So far, no such tools are available in literature due to the fact that imaging of the 3D morphology in high resolution is a difficult task. The first 3D images of photoactive layers in polymer solar cells, gained by means of electron tomography (ET), have been published only recently; see [van Bavel et al. \(2009\)](#) and [Oosterhout et al. \(2009\)](#).

In the present paper, such 3D images are used to fit our model to real data. The model then helps to get a better insight into the impact of morphology on the performance of polymer solar cells and, simultaneously, it can be used for virtual scenario analyses, where model-based morphologies of solar cells are simulated to identify polymer solar cells with improved nanostructures.

The model developed in this paper is based on methods from stochastic geometry and spatial statistics; see [Kendall and Molchanov \(2010\)](#) and [Gelfand et al. \(2010\)](#) for comprehensive surveys on recent results in these fields. In particular, stationary marked point processes are considered as models for complex point patterns extracted from ET images, where the points are associated with additional information, so-called "marks."

Note that point processes in 3D have been used for many years to analyze geometrically complex point patterns; see, for example, [Baddeley et al. \(1987\)](#). More recently, further case studies in 3D point process modeling have been performed, for example, in [Ballani, Daley and Stoyan \(2005\)](#), [Beil et al. \(2005\)](#) and [Stoica, Gregori and Mateu \(2005\)](#); see also [Baddeley et al. \(2006\)](#). Besides, there are many monographs dealing with point processes in multidimensional spaces and their statistical inference and simulation. We refer, for instance, to [Daley and Vere-Jones \(2008\)](#), [Diggle \(2003\)](#), [Illian et al. \(2008\)](#), [Møller and Waagepetersen \(2004\)](#), as well as [Stoyan, Kendall and Mecke \(1995\)](#).

The paper is organized as follows. Section 2 briefly describes the considered solar cells and the corresponding image data on which the model is based. In particular, in Section 2.3, the main ideas of a multi-scale approach to the segmentation of 3D images are summarized, which has been developed recently in [Thiedmann et al. \(2011\)](#). The crucial step of this approach is to find an efficient representation of the binarized and morphologically smoothed images by unions of overlapping spheres.

Then, in Section 3, the spatial stochastic model for the ZnO phase is introduced, separately for morphologically smoothed ZnO domains (macro-scale) and for those parts representing the difference between the smoothed and nonsmoothed binary images (micro-scale). Based on unions of overlapping spheres representing the ZnO domains, that is, marked point patterns extracted from ET images, a stochastic model is built for the smoothed 3D morphology (macro-scale) of the

photoactive layers considered in this paper. Since a strong correlation of midpoints of spheres in z -direction is observed, we propose a multi-layer approach considering sequences of correlated 2D point processes to model the 3D point patterns of midpoints. The members of these sequences belong to a suitably chosen class of planar Poisson cluster processes, being parallel to the x - y -plane. In particular, a generalized version of Matérn cluster processes is considered, where the cluster points are scattered in uniformly oriented ellipses around their cluster centers (Section 3.1.1). To model the 3D point patterns of midpoints, a Markov chain with stationary initial distribution is constructed, which consists of highly correlated Matérn cluster processes (Section 3.1.2). It can be seen as a stationary point process in 3D, where the radii of spheres are considered as marks of this point process (Section 3.1.3). Subsequently, a spatial stochastic model for the micro-scale part of the morphological structure is developed (Section 3.2). It is used to invert morphological smoothing and completes our model for the 3D morphology of hybrid polymer-ZnO solar cells. Furthermore, a method to fit model parameters to real image data is proposed.

Section 4 deals with model validation. To evaluate the goodness of fit, we compare model characteristics which have been computed from real and simulated data, respectively, like the volume fractions of voxels contributing to monotonous percolation pathways through the photoactive layer, the distribution of spherical contact distances, and the probabilities of exciton quenching. These characteristics have already been considered in [Oosterhout et al. \(2009\)](#), since they are strongly related with the performance of solar cells. Finally, Section 5 concludes and provides a short outlook regarding possible future research.

2. Polymer solar cells. In this section some necessary background information regarding the functionality of polymer solar cells is provided, together with corresponding image data on which the model is based.

2.1. Photoactive layers. We consider photoactive layers of hybrid polymer zinc oxide (ZnO) solar cells where the two solid phases play the role of a polymeric electron donor, consisting of, for example, poly(3-hexylthiophene), and an inorganic ZnO-electron acceptor, respectively. Upon exposure to light, photons are absorbed in the polymer phase and so-called “excitons,” that is, photoexcited electron-hole pairs, evolve. Excitons are neutral quasi-particles which diffuse inside the polymer phase within a limited lifetime; see [Shaw, Ruseckas and Samuel \(2008\)](#). If an exciton reaches the interface to the ZnO phase, it is split up into a free electron (negative charge) in the ZnO and a hole (positive charge) in the polymer phase. This process is commonly referred to as quenching, because it reduces the intrinsic fluorescent decay of the exciton in the polymer. Provided that the electrons in the ZnO phase and the holes in the polymer phase reach the electrodes at the top and bottom of the photoactive layer, respectively, photocurrent is generated. A schematic illustration of the morphology of photoactive layers in hybrid

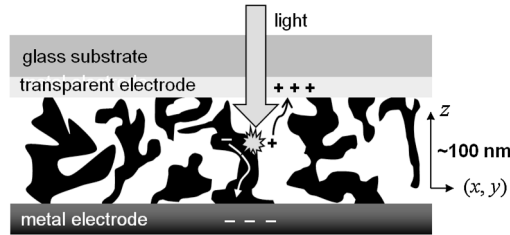


FIG. 1. Schematic layout of a polymer-ZnO thin film solar cell, showing the percolation of photo-generated holes (+) and electrons (-).

polymer-ZnO solar cells is shown in Figure 1, where the electrodes are supposed to be parallel to the x - y -plane. For further information about polymer solar cells and the physical processes therein we refer, for example, to Brabec, Scherf and Dyakonov (2008).

Note that the extent of blending of the two materials has a large impact on the efficiency of these solar cells, because not all excitons are quenched due to their limited lifetimes. Thus, a morphology as displayed in Figure 1, where both materials are mixed intimately, is desirable since the excitons are likely to reach the interface and charges can be generated. In other words, for a morphology which would be ideal with respect to this aspect of functionality, each location of the polymer phase should have a distance to the ZnO phase that is smaller than the diffusion length of excitons. For each location within the polymer phase, the fraction of excitons reaching the interface is called the quenching probability at this location. The mean of these quenching probabilities, that is, the quenching probability at a randomly chosen location of the polymer phase, is called the quenching efficiency.

Furthermore, the existence of unhindered percolation pathways within both phases, ZnO and polymer, is crucial since the generated charges have to be transported to the electrodes throughout the phases. Because of the electric field between the electrodes, these pathways should be preferably monotonous. Hence, to obtain solar cells with high efficiency, an intimately mixed morphology with monotonous percolation pathways for both charge carriers is desirable and should be taken into account when producing devices. The stochastic model developed in the present paper will be used to identify morphologies with improved efficiency by generating virtual morphologies and investigating the transport processes of electrons and excitons, respectively. This will be the subject of a forthcoming paper.

2.2. Electron tomography images. The image data have been gained by electron tomography (ET); see van Bavel et al. (2009) and Oosterhout et al. (2009). In particular, we consider images for three devices with different thicknesses of the photoactive layers: 57 nm, 100 nm and 167 nm. For each of the three thicknesses,

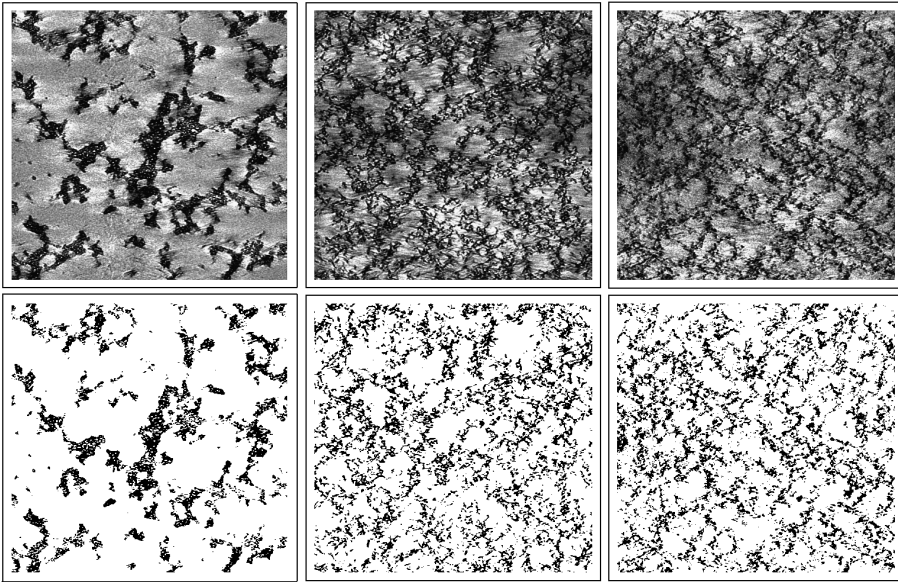


FIG. 2. 2D images of hybrid polymer-ZnO solar cells; first column: 57 nm, second: 100 nm, third: 167 nm; first row: original grayscale images, second: binarized images.

the 3D ET images are given as stacks of 2D grayscale images (being parallel to the x - y -plane, say), which are numbered according to their location in z -direction. The sizes of these images in the x - y -plane are 934×911 voxels for the 57 nm film, and 942×911 voxels for the other two thicknesses. Each voxel represents a cube with side length of 0.71 nm.

Figure 2 shows representative 2D slices for the three film thicknesses, where the darker parts of the images represent the ZnO phase due to a higher electron density compared to polymer. The images displayed in Figure 2 indicate clear structural differences for the three films. With increasing layer thickness, the separated domains of polymer and ZnO are getting finer. In particular, the thinnest film, that is, the photoactive layer with thickness of 57 nm, features large domains of both polymer and ZnO. The stochastic 3D model to be fitted takes these morphological differences into account. More precisely, the model type will be the same for all three layer thicknesses. Only the values of some model parameters will be different for the varying morphologies; see Section 3 below.

To develop a stochastic model for the 3D morphology of hybrid polymer-ZnO solar cells, the 3D ET grayscale images have to be binarized appropriately. Binarization is necessary since we need to decide which voxels are classified as polymer and which as ZnO. An elementary approach to binarize grayscale images is to use a global threshold: voxels are set to white (polymer) if their grayscale value exceeds a certain threshold, and are otherwise set to black (ZnO). However, it is difficult to find a single global threshold to binarize the ET images because of the irreg-

ular brightness of these images. Thus, instead of considering global thresholds, a method of adaptive thresholding has been used for binarization; see Thiedmann et al. (2011). This method is based on techniques of Yanowitz and Bruckstein (1989) and Blayvas, Bruckstein and Kimmel (2006), where the main idea is to construct a threshold surface which is location-dependent and takes local conditions like overexposure or underexposure into account. Examples of binarizing the ET images by adaptive thresholding are displayed in Figure 2.

2.3. Segmentation of binarized images. In this section we briefly summarize the main ideas of a multi-scale approach to the segmentation of 3D images, which has been developed recently in Thiedmann et al. (2011). The crucial step is to find an efficient representation of the binarized and morphologically smoothed images by unions of overlapping spheres.

Let B denote the ZnO phase of the binarized images. Since the morphology of the set B is rather complex (see Figure 2), it is difficult to describe this morphology directly, just by a single stochastic model. We therefore developed a multi-scale approach to represent the ZnO phase by different structural components. Each of them will be described separately by suitably chosen stochastic models. More precisely, we distinguish between a macro-scale component of the binarized ET images, which is obtained by morphological smoothing, and several micro-scale components, which consist of those voxels that have been misspecified by the morphological smoothing; see Figure 3. The intention of morphological smoothing is to reduce the structural complexity of the binarized ET images, that is, to omit very fine structural components such as “thin ZnO branches,” that is, thin ZnO parts connected to larger ZnO domains, “isolated ZnO particles,” that is,

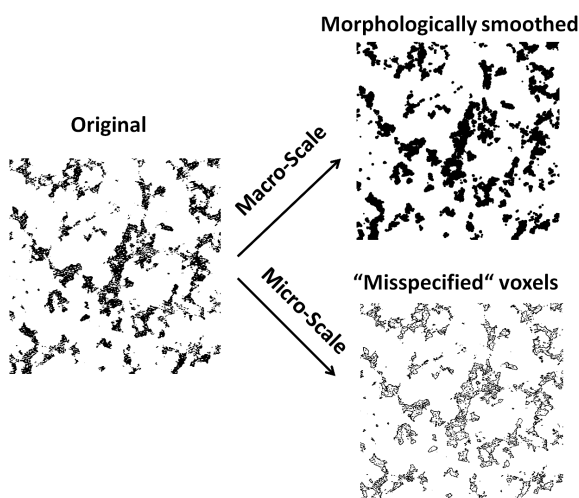


FIG. 3. Original image split up into structural components at two different scales.

small ZnO particles in the polymer domains, and “polymeric holes,” that is, small polymeric particles inside the ZnO domains. The morphological transformations which we use for smoothing the ZnO phase B of the original binarized ET images are twofold: “dilation” and “erosion.” The morphologically smoothed version of the set B will thus be denoted by B'' .

In the next step a stochastic algorithm [see Thiedmann et al. (2011)] is used to efficiently represent the set B'' by a union of spheres, which is denoted by B''' . This leads to an enormous data reduction. Another advantage of this representation of the set B'' by unions of spheres is that it allows the interpretation of the morphologically smoothed ZnO phase as a realization of a marked point process where the midpoints of the spheres are the points and the corresponding radii the marks.

Recall that in the macro-scale component B'' of the binarized ET images as well as in its representation B''' by unions of spheres, some structural details of the original ZnO phase B , like isolated particles, thin branches and polymeric holes, are omitted. Furthermore, the boundaries of ZnO domains are morphologically smoothed and slightly enlarged by dilation. Hence, when comparing the sets B and B''' , we observe that some voxels are misspecified, that is, indicated as ZnO although originally being polymer, and vice versa. The set $B \Delta B''' = (B \cup B''') \setminus (B \cap B''')$ of misspecified voxels is subdivided into several subcomponents, where each of these subcomponents will be modeled separately. First, two main types of misspecifications are distinguished: outer misspecifications and inner misspecifications; see Figure 4. Each ZnO voxel that is not covered by a sphere, that is, belonging to the set $B \setminus B'''$ and therefore constituted as polymer, is called an outer misspecification. Typically, thin branches and isolated ZnO particles are outer misspecifications. On the other hand, each polymer voxel which is covered by a sphere, that is, belonging to $B^c \cap B'''$ and constituted as ZnO, is called an inner misspecification. Inner misspecifications are further subdivided into boundary misspecifications and interior misspecifications. On the one hand, polymer voxels (belonging to B^c), located near the boundary $\partial B''$ of the macro-scale component B'' and covered by a sphere, are called boundary misspecifications. On

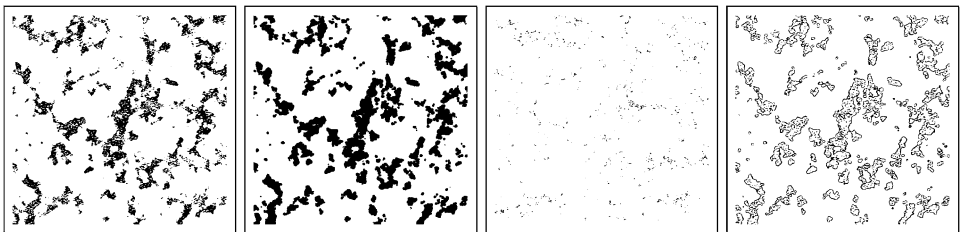


FIG. 4. First: binarized (nonsmoothed) 2D slice of 57 nm file; second: representation by unions of spheres; third: outer misspecifications; fourth: inner misspecifications (boundary and interior).

the other hand, each inner misspecification which is not a boundary misspecification is called an interior misspecification. Typically, polymeric holes belong to interior misspecifications.

3. Stochastic modeling. We now present our approach to stochastic modeling of the 3D nanomorphology of the ZnO phase in photoactive layers with three different thicknesses which are given by the binarized ET images described in Section 2.2. Note that the model type is the same for all three thicknesses, just the fitted values of some model parameters are different. This means, in particular, that our model can be used for computer-based scenario analyses with the general objective of developing improved materials and technologies for polymer solar cells.

In accordance with the multi-scale representation of the ZnO phase which has been described in Section 2.3, we will establish stochastic simulation models separately for the morphologically smoothed ZnO domains represented by unions of overlapping spheres, that is, the macro-scale representation of the ZnO phase, and for the three types of misspecifications, that is, the micro-scale components.

3.1. *Point-process model for systems of overlapping spheres.* To begin with, we develop a point-process model which describes the macro-scale component of the ZnO phase represented by unions of spheres. This model is constructed in several steps. First we consider 2D point processes for those midpoints of spheres which belong to single slices of voxels, being parallel to the x - y -plane. Since a strong correlation of midpoint spheres in z -direction is observed, we propose a multi-layer approach considering sequences of correlated 2D point processes to model the 3D point patterns of midpoints.

The members of these sequences belong to a suitably chosen class of planar Poisson cluster processes. In particular, elliptical Matérn cluster processes are considered, where the cluster points are scattered in ellipses of uniformly distributed orientation around their cluster centers. To model the 3D point patterns of midpoints, a Markov chain with stationary initial distribution is constructed, which consists of highly correlated Matérn cluster processes. It can be seen as a stationary point process in 3D, where the radii of spheres are considered as marks of this point process. The mark correlation functions, which have been computed for the radii of spheres extracted from ET images, show strong positive correlations for small distances between midpoints. Hence, for a given configuration of midpoints, the radii associated with these midpoints are not modeled just by independent marking, but a certain moving-average procedure is proposed. Note that our model of a stationary marked point process in 3D describing the macro-scale component of the ZnO phase is not isotropic. This is in accordance with the nanomorphology observed in the ET images; see [Oosterhout et al. \(2009\)](#).

3.1.1. *Elliptical Matérn cluster processes.* To get an idea which class of point processes is suitable to model the midpoints belonging to the individual slices of voxels, we consider the pair correlation function $g : (0, \infty) \rightarrow (0, \infty)$ of stationary

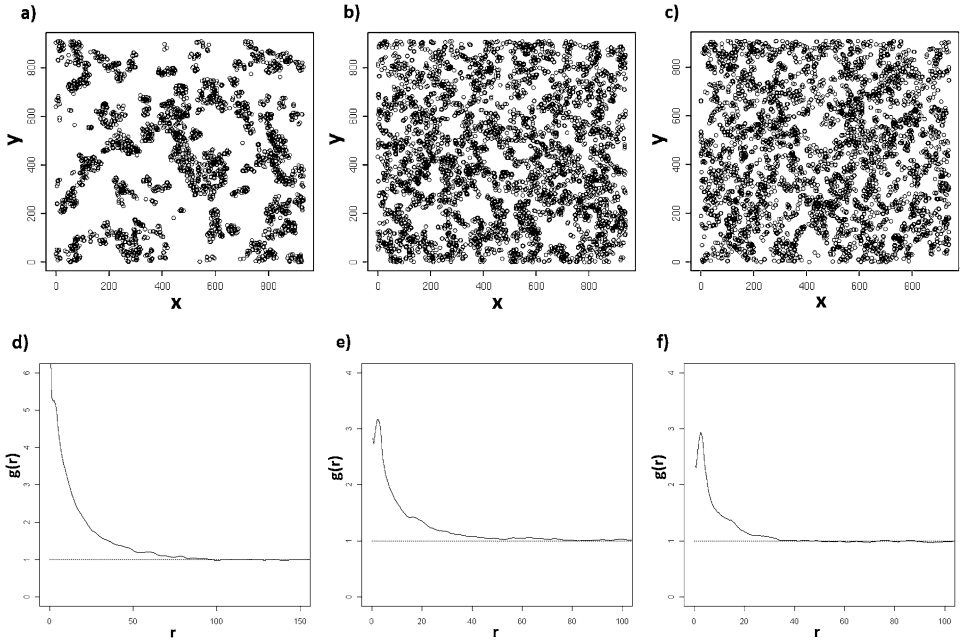


FIG. 5. *Top: point patterns of midpoints in 2D slices (a = 57 nm, b = 100 nm, c = 167 nm); bottom: estimated pair correlation functions (d = 57 nm, e = 100 nm, f = 167 nm).*

and isotropic point processes in \mathbb{R}^2 . Note that $g(r)$ is proportional to the relative frequency of point pairs with distance $r > 0$ from each other; see, for example, Illian et al. (2008). Then, for each of the three photoactive layers with thicknesses of 57 nm, 100 nm, and 167 nm, the values $\widehat{g}(r)$ of the pair correlation function have been estimated for distances r within some interval $(0, r_{\max})$; see Figure 5.

Since $\widehat{g}(r) > 1$ for small $r > 0$, these estimates clearly indicate clustering of points, which can also directly be seen from the point patterns shown in Figure 5. The clusters appearing in these point patterns seem to be located in relatively small (bounded) areas, which corresponds to the fact that $\widehat{g}(r) \approx 1$ for sufficiently large $r > 0$. The shapes of the clusters are not circular, but rather elongated. Hence, we propose to consider Matérn cluster processes, where the cluster points are scattered in ellipses of uniformly distributed orientation around their cluster centers.

This class of (elliptical) Matérn cluster processes in \mathbb{R}^2 can be described by a vector of four parameters: $(\lambda_c, \lambda_d, a, b)$, where λ_c is the intensity of the stationary Poisson point process $\{T_n, n \geq 1\}$ of cluster centers, a and b with $a > b > 0$ are the semi-axes of (random) ellipses $\mathcal{E}_{a,b}(T_n, \zeta_n) \subset \mathbb{R}^2$ centered at the points T_n of the Poisson process $\{T_n\}$ of cluster centers and rotated around T_n by random angles ζ_n which are independent and uniformly distributed on the interval $[0, \pi)$, and λ_d is the intensity of the stationary Poisson processes $\{S_{ni}, i \geq 1\}$ of cluster members which are released by the cluster centers T_n within the ellipses

$\mathcal{E}_{a,b}(T_n, \zeta_n)$. The Matérn cluster process is then defined as the random point pattern $\{S_n\}$ given by $\{S_n\} = \bigcup_{n=1}^{\infty} (\{S_{ni}, i \geq 1\} \cap \mathcal{E}_{a,b}(T_n, \zeta_n))$, where the sequences $\{\zeta_n\}$, $\{T_n\}$, $\{S_{1i}\}$, $\{S_{2i}\}, \dots$ are assumed to be independent.

3.1.2. *Markov chain of Matérn cluster processes.* There are strong similarities between consecutive 2D slices in terms of a high correlation of midpoint locations in z -direction as well as approximately equal numbers of points. Figure 6 shows a series of such consecutive 2D slices from the 57 nm data set.

As a consequence, it is not suitable to model the stacks of these 2D point patterns by sequences of independent Matérn processes. But the (vertical) correlation structure visualized in Figure 6 can be taken into account by considering a Markov chain of Matérn processes. This allows us to model small displacements of clusters when passing from slice to slice. Furthermore, “births” and “deaths” of clusters in z -direction can also be modeled in this way. In other words, we consider a certain class of spatial birth-and-death processes with random displacement of points; see, for example, Møller and Waagepetersen (2004).

For each integer $z \geq 1$, let $\{B_n^{(z)}, n \geq 1\}$ be a stationary Poisson point process in \mathbb{R}^2 with intensity λ'_c such that $0 < \lambda'_c < \lambda_c$, and let $\{\delta_n^{(z)}, n \geq 1\}$ be an independent and identically distributed (i.i.d.) sequence of Bernoulli random variables, which is independent of $\{B_n^{(z)}\}$, where $P(\delta_n^{(z)} = 1) = p$ for some $p \in (0, 1)$. Note that $\{B_n^{(z)}\}$ and $\{\delta_n^{(z)}\}$ will be used in order to model “births” and “deaths” of cluster centers, respectively.

For each integer $z \geq 1$, an i.i.d. sequence $\{D_n^{(z)}\}$ of random displacement vectors $D_1^{(z)}, D_2^{(z)}, \dots$ with values in \mathbb{R}^2 is considered, which is independent of $\{B_n^{(z)}\}$ and $\{\delta_n^{(z)}\}$. We assume that the random vectors $D_1^{(z)}, D_2^{(z)}, \dots$ are uniformly distributed in the set $b(o, r'') \setminus b(o, r')$, where r' and r'' denote the size of minimum and maximum displacement, respectively; $0 < r' < r''$.

Then, a (stationary) Markov chain $\{\{S_n^{(z)}, z \geq 1\}$ of Matérn processes can be constructed as follows. For $z = 1$, let $\{S_n^{(1)}\}$ be an elliptical Matérn cluster process

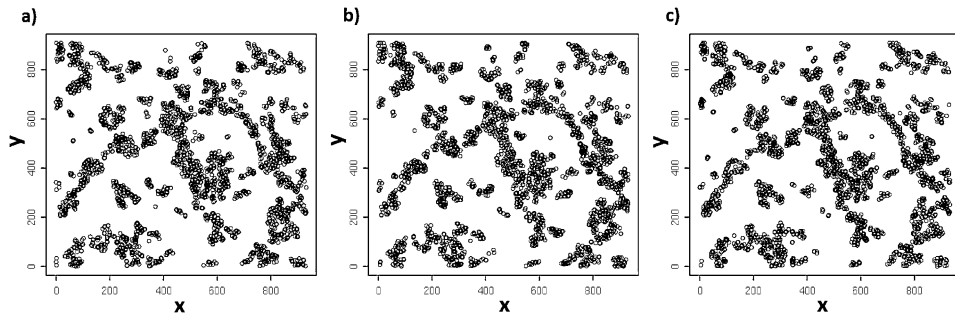


FIG. 6. Point patterns of midpoints for successive 2D-slices from the 57 nm data set (a = slice 35, b = slice 36, c = slice 37).

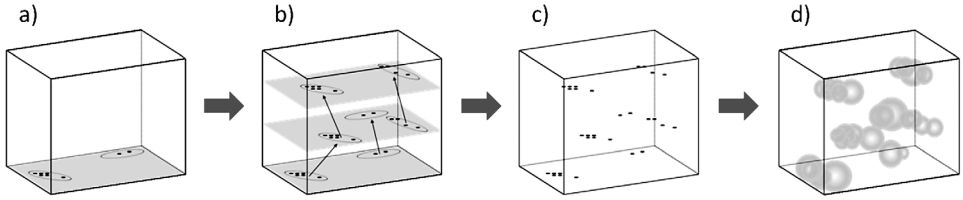


FIG. 7. (a) initial 2D point pattern; (b) displacement of cluster centers, including “birth” and “death;” (c) 3D point pattern; (d) union of spheres.

as introduced in Section 3.1.1, that is, $\{S_n^{(1)}\} = \bigcup_{n=1}^{\infty} (\{S_{ni}, i \geq 1\} \cap \mathcal{E}_{a,b}(T_n, \zeta_n))$. Assume that the “birth rate” λ'_c and the “survival probability” p satisfy $\lambda_c p + \lambda'_c = \lambda_c$, where λ_c is the intensity of the Poisson process $\{T_n\}$ of cluster centers. For $z = 2$, the Poisson process $\{T_n^{(2)}\}$ of cluster centers is then given by $\{T_n^{(2)}, n \geq 1\} = \bigcup_{j: \delta_j^{(1)}=1} \{T_j^{(1)} + D_j^{(1)}\} \cup \{B_n^{(1)}, n \geq 1\}$. The Poisson process $\{T_n^{(3)}\}$ is constructed in the same way as $\{T_n^{(2)}\}$, that is,

$$\{T_n^{(3)}, n \geq 1\} = \bigcup_{j: \delta_j^{(2)}=1} \{T_j^{(2)} + D_j^{(2)}\} \cup \{B_n^{(2)}, n \geq 1\},$$

and so on; see also Figure 7. The Matérn processes $\{S_n^{(2)}\}, \{S_n^{(3)}\}, \dots$ are built similarly to the construction of $\{T_n^{(2)}\}, \{T_n^{(3)}\}, \dots$. For example, $\{S_n^{(2)}\}$ is given by

$$\begin{aligned} \{S_n^{(2)}\} = & \bigcup_{j: \delta_j^{(1)}=1} (\{S_{ji} + D_j^{(1)}, i \geq 1\} \cap \mathcal{E}_{a,b}(T_j^{(1)} + D_j^{(1)}, \zeta_j)) \\ & \cup \bigcup_{n=1}^{\infty} (\{S_{ni}^{(1)}, i \geq 1\} \cap \mathcal{E}_{a,b}(B_n^{(1)}, \zeta_n^{(1)})), \end{aligned}$$

where the sequences $\{\zeta_n^{(1)}\}, \{S_{1i}^{(1)}\}, \{S_{2i}^{(1)}\}, \dots$ are defined in the same way as $\{\zeta_n\}, \{S_{1i}\}, \{S_{2i}\}, \dots$ introduced in Section 3.1.1.

The Markov chain $\{\{S_n^{(z)}\}, z \geq 1\}$ of Matérn processes introduced above can be seen as a stationary point process in 3D. It possesses seven (free) parameters: $\lambda_c, \lambda_d, a, b$ describing its initial distribution, and p, r', r'' describing the transitions from step to step, whereas the “birth intensity” λ'_c of (new) cluster centers is given by $\lambda'_c = \lambda_c(1 - p)$. It turned out that suitable choices for r', r'' are the values of $r' = \sqrt{2}/2$ and $r'' = 1.5$. This means that the uniform distribution of the displacement vectors $D_1^{(z)}, D_2^{(z)}, \dots$ is implemented as (discrete) uniform distribution on the 8-neighborhood in the considered slice of voxels. Techniques for fitting the remaining five parameters of the Markov chain $\{\{S_n^{(z)}\}, z \geq 1\}$ are discussed in Section 3.1.4.

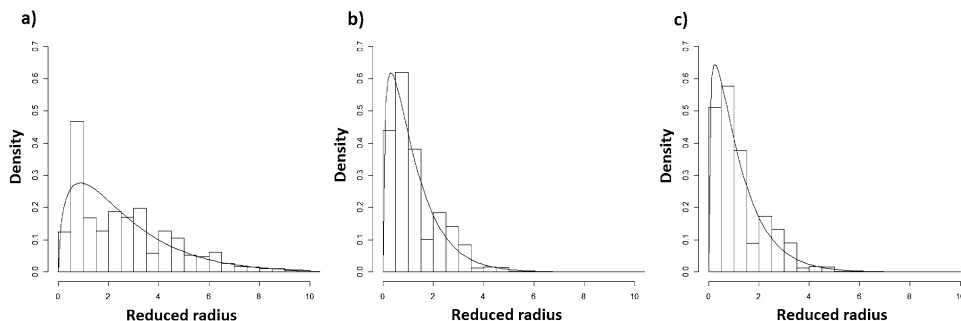


FIG. 8. Histograms of reduced radii and fitted gamma distributions (solid lines); $a = 57$ nm, $b = 100$ nm, $c = 167$ nm.

3.1.3. *Modeling the radii of spheres.* To get an idea which class of mark distributions is suitable to model the radii of spheres, we computed histograms of radii which have been extracted from the ET images for each of the three photoactive layers with thicknesses of 57 nm, 100 nm and 167 nm. Recall that in the sphere-putting algorithm mentioned in Section 2.3 we only consider spheres with a minimum radius of $\sqrt{3}$ voxel sizes. Hence, instead of computing histograms for the original radii, say, r_1, r_2, \dots , we computed histograms for correspondingly reduced radii r'_1, r'_2, \dots , where $r'_n = r_n - \sqrt{3}$. It turns out that for all three film thicknesses, gamma distributions can be fitted quite nicely to the histograms of reduced radii; see Figure 8. The parameters k and θ of these gamma distributions $\Gamma(k, \theta)$ have been estimated using the method of moments; see Table 1.

The mark correlation function of stationary marked point processes is considered, which describes the spatial correlations of pairs of marks, depending on the distance vector of the corresponding pairs of points; see, for example, Illian et al. (2008). For each representation of the three photoactive layers by unions of overlapping spheres, the values $\hat{\kappa}(r)$ of this function have been estimated for distance vectors of length r . They show strong positive correlations for radii corresponding to pairs of midpoints with small distances from each other; see Figure 9.

Thus, for a given configuration $\{s_n^{(z)}, n, z \geq 1\}$ of midpoints, the radii $\{R_n^{(z)}, n, z \geq 1\}$ associated with these midpoints are not modeled just by independent marking, but the following moving-average procedure is proposed. For some $m \geq 1$, let

TABLE 1
Parameters for gamma distributions of radii

Parameter	57 nm film	100 nm film	167 nm film
k	1.51	1.36	1.26
θ	1.73	0.88	0.93

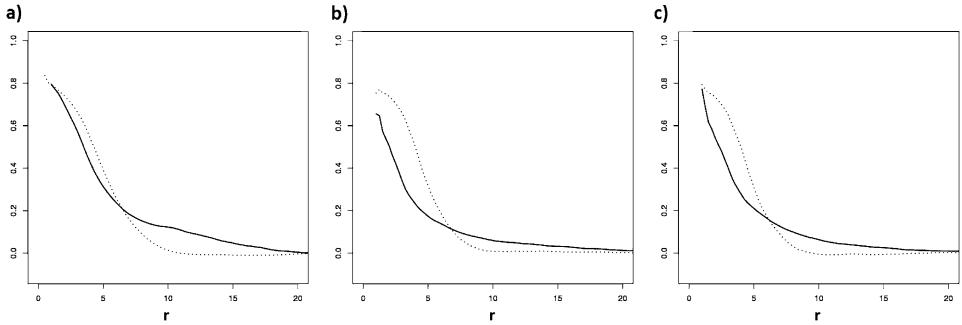


FIG. 9. Comparison of estimated (solid) and simulated (dotted) mark correlation functions for arbitrary distance vectors in 3D of length r ; a = 57 nm, b = 100 nm, c = 167 nm.

$\{\tilde{R}_n^{(z)}, n, z \geq 1\}$ be an i.i.d. sequence of $\Gamma(k/m, \theta)$ -distributed random variables, and let $(z_1, n_1), \dots, (z_m, n_m)$ for each index (z, n) denote the indices of the m nearest neighbors $s_{n_1}^{(z_1)}, \dots, s_{n_m}^{(z_m)}$ of $s_n^{(z)}$ [including the point $s_n^{(z)}$ itself]. Then, the radius $R_n^{(z)} = \sqrt{3} + \tilde{R}_{n_1}^{(z_1)} + \dots + \tilde{R}_{n_m}^{(z_m)}$ is assigned to the midpoint $s_n^{(z)}$. The reduced radius $R_n^{(z)} - \sqrt{3}$ obtained in this way is $\Gamma(k, \theta)$ -distributed. It turned out that for $m = 4$, the estimated mark correlation functions computed from real data (i.e., original point pattern and original radii) show a good resemblance to their simulated counterparts (i.e., original point pattern and simulated radii) for all three thicknesses of photoactive layers; see Figure 9.

3.1.4. *Model fitting for midpoints of spheres.* The (overall) intensity of midpoints of spheres, that is, the intensity λ of the stationary point process $\{S_n^{(z)}, z, n \geq 1\}$ can be easily estimated by $\hat{\lambda} = \#\{S_n^{(z)} : S_n^{(z)} \in W\} / |W|$, where $\#\{S_n^{(z)} : S_n^{(z)} \in W\}$ is the total number of midpoints in the sampling window $W \subset \mathbb{R}^3$ and $|W|$ denotes the volume of W . Using this formula, the following values have been obtained for the spheres extracted from the binarized ET images: $\hat{\lambda} = 1.83 \cdot 10^{-3}$ for the 57 nm film, $\hat{\lambda} = 5.29 \cdot 10^{-3}$ for the 100 nm film, and $\hat{\lambda} = 5.15 \cdot 10^{-3}$ for the 167 nm film.

Note that $\lambda = \lambda_c \lambda_d |\mathcal{E}_{a,b}|$, where $|\mathcal{E}_{a,b}|$ denotes the area of an ellipse with semi-axes a and b . Therefore, in order to determine λ_d , the estimator $\hat{\lambda}_d = \hat{\lambda} (\hat{\lambda}_c |\mathcal{E}_{\hat{a}, \hat{b}}|)^{-1}$ can be used, provided that an estimator $\hat{\lambda}_c$ for the intensity λ_c of cluster centers as well as estimators \hat{a} and \hat{b} for the semi-axes a and b are available. Similarly to the estimation of λ_d discussed above, the estimator $\hat{\lambda}'_c = \hat{\lambda}_c (1 - \hat{p})$ for the birth rate λ'_c can be considered, provided that estimators $\hat{\lambda}_c$ and \hat{p} for λ_c and p are given.

Finally, we derive a so-called minimum-contrast estimator for the vector of the remaining four parameters λ_c, a, b and p , where we traverse the parameter space of these parameters. This means that for each vertex of a certain lattice of parameter vectors (λ_c, a, b, p) , the 3D point process $\{S_n^{(z)}, z, n \geq 1\}$ of midpoints described

in Sections 3.1.1 and 3.1.2 is simulated in the sampling window W and gamma-distributed radii are added according to the moving average procedure described in Section 3.1.3. Then, structural characteristics of simulated unions of spheres are compared with corresponding structural characteristics of unions of spheres extracted from binarized ET images.

In particular, consider the empirical distribution function $\widehat{F}^{SCD}: [0, \infty) \rightarrow [0, 1]$ of spherical contact distances from polymer to ZnO, computed for the macro-scale component of binarized ET images, and let $\widehat{F}^{(x)}, \widehat{F}^{(y)}, \widehat{F}^{(z)}: [0, \infty) \rightarrow [0, 1]$ denote the empirical chord-length distribution functions of the ZnO domains in these images along the x -, y - and z -axis, respectively. More information on spherical contact distance distributions and chord length distributions can be found in Ohser and Mücklich (2000) and in Stoyan, Kendall and Mecke (1995). Consider the volume fraction \widehat{V} of ZnO, computed for the macro-scale component of binarized ET images, and let \widehat{V}' denote the volume fraction of those ZnO voxels of the macro-scale component contributing to percolation pathways (monotonous and nonmonotonous) through the photoactive layer.

Let $F_{\lambda_c, a, b, p}^{SCD}, F_{\lambda_c, a, b, p}^{(x)}, F_{\lambda_c, a, b, p}^{(y)}, F_{\lambda_c, a, b, p}^{(z)}$ be the corresponding distribution functions and $V_{\lambda_c, a, b, p}, V'_{\lambda_c, a, b, p}$ the volume fractions, respectively, obtained from simulated 3D morphologies in dependency of λ_c, a, b and p . Then, each solution $(\widehat{\lambda}_c, \widehat{a}, \widehat{b}, \widehat{p})$ of the minimization problem

$$\begin{aligned} (\widehat{\lambda}_c, \widehat{a}, \widehat{b}, \widehat{p}) = \operatorname{argmin}_{\lambda_c, a, b, p} & (w^{SCD} \|\widehat{F}^{SCD} - F_{\lambda_c, a, b, p}^{SCD}\| + w^{(x)} \|\widehat{F}^{(x)} - F_{\lambda_c, a, b, p}^{(x)}\| \\ & + w^{(y)} \|\widehat{F}^{(y)} - F_{\lambda_c, a, b, p}^{(y)}\| + w^{(z)} \|\widehat{F}^{(z)} - F_{\lambda_c, a, b, p}^{(z)}\| \\ & + w^{(V)} |\widehat{V} - V_{\lambda_c, a, b, p}| + w^{(V')} |\widehat{V}' - V'_{\lambda_c, a, b, p}|) \end{aligned}$$

is called a minimum-contrast estimator for (λ_c, a, b, p) , where $w^{SCD}, w^{(x)}, w^{(y)}, w^{(z)} \geq 0$ and $w^{(V)}, w^{(V')} \geq 0$ are some weights such that $w^{SCD} + w^{(x)} + w^{(y)} + w^{(z)} w^{(V)} + w^{(V')} = 1$, and $\|\widehat{F} - F\| = \sup_{t \in \mathbb{R}} |\widehat{F}(t) - F(t)|$ denotes the Kolmogorov distance of \widehat{F} and F .

The minimization problem described above is solved numerically, that is, only a relatively coarse lattice of parameter vectors (λ_c, a, b, p) can be taken into account. Table 2 summarizes the results obtained in this way, where we put $w^{SCD} = w^{(V)} = w^{(V')} = 1/4$ and $w^{(x)} = w^{(y)} = w^{(z)} = 1/(3 \cdot 4) = 1/12$. The results shown in Table 2 nicely reflect the main structural differences and similarities of the patterns of sphere midpoints for the 57 nm, 100 nm, and 167 nm films: The estimated values for λ_c, a and b indicate that the 57 nm film has fewer, but larger clusters of midpoints than the 100 nm and 167 nm films, whereas the intensity λ_d of cluster members is similar for all three films; see also Figure 5. The survival probability p is close to 1 and, therefore, the birth rate λ'_c is much smaller than the intensity λ_c of “old” cluster centers; see Figure 6.

TABLE 2
Parameters for 3D point processes of midpoints

Parameter	57 nm film	100 nm film	167 nm film
λ_c	9.0E-5	1.25E-3	1.00E-3
a	45	22	24
b	15	6	10
p	0.987	0.991	0.977
λ_d	9.59E-3	10.0E-3	6.83E-3
λ'_c	1.17E-6	1.17E-5	2.34E-5

We also remark that the method of statistical model-fitting explained in this section leads to a relatively high degree of visual coincidence between simulated and real ET images; see Figure 10. A more formal approach to model validation will be given later on in Section 4.

3.2. *Stochastic modeling of clusters of misspecified voxels.* We now develop a modeling approach for the micro-scale part of the morphological structure. It is used to stochastically invert the morphological smoothing and completes our model for the 3D morphology of hybrid polymer-ZnO solar cells. The micro-scale morphology is modeled separately for each of the three types of misspecifications, that is, the micro-scale components of outer, boundary, and interior misspecifications mentioned in Section 2.3.

3.2.1. *Outer misspecifications.* Recall that each ZnO voxel that is not covered by a sphere, and therefore constituted as polymer, is said to be an outer misspecification. They typically form thin branches or small isolated ZnO particles. In the present section, a stochastic model is proposed for the locations and sizes of clusters of outer misspecifications, that is, the connected components of the set $B \setminus B'''$

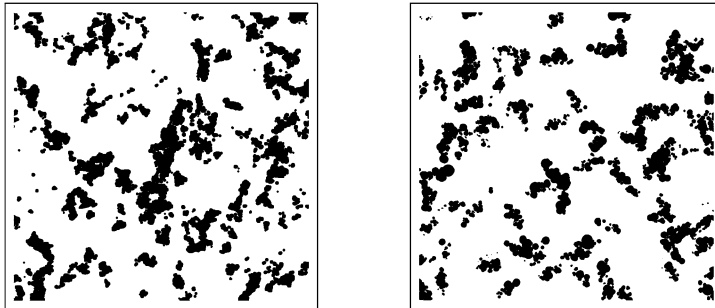


FIG. 10. Left: 2D slice of the morphologically smoothed 57 nm film, right: 2D slice of a simulated union of overlapping spheres, drawn from the fitted 3D model.

introduced in Section 2.3. We first consider this kind of misspecification, because it influences the “correction” of boundary misspecifications which will be described in Section 3.2.2 below.

We assume that the centers of gravity of clusters of outer misspecifications form a Cox point process, which is also called a doubly stochastic Poisson process in literature. The cluster sizes are considered as marks. In particular, under the condition that a realization $\{(s_n^{(z)}, r_n^{(z)})\}$ of the (marked) point-process model $\{(S_n^{(z)}, R_n^{(z)}), n, z \geq 1\}$ introduced in Section 3.1 is given which describes the macro-scale component of the ZnO phase represented by the union of spheres $\xi = \bigcup_{n,z \geq 1} b(s_n^{(z)}, r_n^{(z)})$, we assume that the centers of gravity of clusters of outer misspecifications can be described by an inhomogeneous Poisson process. Its (conditional) intensity $\lambda(x)$ at location $x \in \mathbb{R}^2$ depends on the distance $\delta_\xi(x) = \inf\{|x - y| : y \in \xi\}$ between x and the union of spheres ξ , where we put $\lambda(x) = 0$ if $\delta_\xi(x) = 0$.

The intensity $\lambda(x)$ at locations $x \in \mathbb{R}^2$ with $\delta_\xi(x) > 0$ can be estimated by analyzing the centers of gravity of clusters of outer misspecifications in the set $B \setminus B'''$ extracted from binarized ET images. In particular, for any $d_l, d_u > 0$ with $d_l < d_u$, the (average) intensity $\lambda_{[d_l, d_u]}$ of centers of gravity at locations $x \in \mathbb{R}^2$ with $\delta_\xi(x) \in [d_l, d_u)$ can be estimated by

$$\hat{\lambda}_{[d_l, d_u]} = \frac{\text{number of centers of gravity with distance to } B''' \text{ between } d_l \text{ and } d_u}{\text{number of voxels with distance to } B''' \text{ between } d_l \text{ and } d_u}.$$

Examples of results for $\hat{\lambda}_{[d_l, d_u]}$ computed from ET images are given in Table 3. For all three film thicknesses the estimated intensity $\hat{\lambda}_{[d_l, d_u]}$ decreases with increasing distance to the macro-scale component B''' of the ZnO phase.

We assume that within shells around the set $\xi = \bigcup_{n,z \geq 1} b(s_n^{(z)}, r_n^{(z)})$ with distance to ξ in the distance class $[d_l, d_u)$, the intensity of centers of gravity of outer misspecifications is constant and given by $\lambda_{[d_l, d_u]}$. We assume that the clusters of

TABLE 3
Model parameters for outer misspecifications

		57 nm	100 nm	167 nm
Intensity	$\lambda_{[0,2)}$	1.78E-3	5.25E-3	5.70E-3
	$\lambda_{[2,4)}$	5.22E-4	4.31E-4	6.88E-4
	$\lambda_{[4,6)}$	1.81E-4	1.80E-4	4.48E-4
	$\lambda_{[6,8)}$	1.04E-4	1.10E-4	3.28E-4
	$\lambda_{[8,10)}$	6.90E-5	6.06E-5	2.31E-4
Slope	α	-0.90	-0.67	-1.13
Axis intercept	β	86.45	33.62	30.92
Variance	σ^2	1,889.5	114.6	63.9

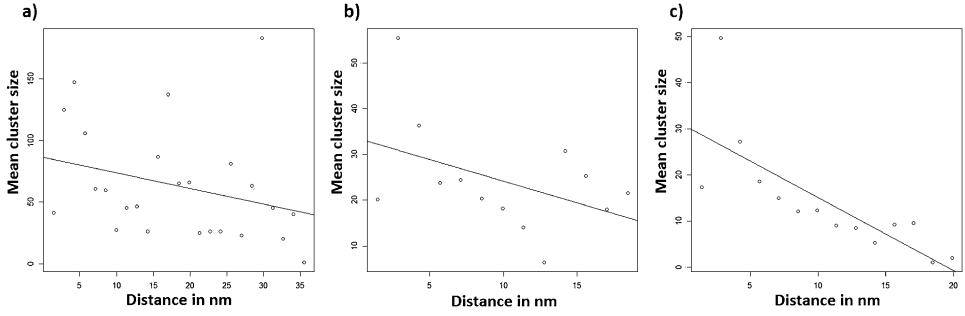


FIG. 11. Mean cluster sizes of outer misspecifications, depending on their distance from the set B''' ; $a = 57$ nm, $b = 100$ nm, $c = 167$ nm.

outer misspecifications are spheres, the radii of which are given in the following way. It turned out that not only the intensity of centers of gravity, but also the cluster sizes observed in binarized ET images, depend on the distances of centers of gravity to the set B''' . In particular, the cluster sizes seem to have a tendency to decrease with increasing distance to the set B''' ; see Figure 11, where the estimated mean values for the radii of the considered distance classes are shown.

To integrate this dependency into our simulation model, we fit regression lines to the point clouds shown in Figure 11, that is, we assume that the points in this figure can be seen as realizations of random variables Y_i satisfying the linear relation $Y_i = \alpha x_i + \beta + \varepsilon_i$, where $x_i = (d_l^{(i)} + d_u^{(i)})/2$ is the midpoint of the i th distance class $[d_l^{(i)}, d_u^{(i)})$ and ε_i is a random error term. The parameters α and β of this regression line are estimated by the method of least squares. As can be seen in the plots of Figure 11, a linear model shows just the trend but is not a perfectly fitting model for describing the cluster sizes in dependence on their distances to the macro-scale component B''' in the ZnO phase. Hence, we additionally consider the residua ε_i in the linear regression model, where we assume that they follow a normal distribution with expectation 0 and variance σ^2 . The estimated values obtained for slope α , intercept β of y -axis, and variance σ^2 of the residua are given in Table 3. To ensure a positive size of each simulated cluster, we reject negative sizes and generate new realizations as long as a positive cluster size is sampled. For simulated clusters of outer misspecifications with a greater distance from the set ξ than the intercept of the fitted regression line with the x -axis, we put the cluster size equal to zero. This is in accordance with real data, because in the binarized ET images such clusters of outer misspecifications do not occur. In the following, by ξ' we will denote a realization of the model with included outer misspecifications.

3.2.2. Boundary misspecifications. After adding the outer misspecifications to our model as described in the previous section, we now develop an algorithm to remove the so-called boundary misspecifications, which primarily result from the

TABLE 4
Fractions of boundary misspecifications in consecutive shells (given in %)

	57 nm		100 nm		167 nm	
	ET data	Simulation	ET data	Simulation	ET data	Simulation
1st shell	87	72	60	67	60	64
2nd shell	74	70	0	0	0	0
3rd shell	71	68	0	0	0	0
4th shell	0	0	0	0	0	0

dilation of the ZnO domains; see Section 2.3. Recall that we defined the boundary misspecifications as those misspecified voxels within some outer shells of the set B''' , that is, the union of spheres representing the morphologically smoothed ZnO phase. The first shell is defined as the set of voxels of B''' , with a distance to $W \setminus B'''$ smaller or equal than 1. In general, the $(i + 1)$ th shell, $i = 1, 2, 3, \dots$, is defined as the set of voxels of B''' with a distance to $W \setminus B'''$ in $(i, i + 1]$.

Table 4 displays the percentage of misspecified boundary voxels in the different outer shells of B''' . Note that boundary misspecifications only occur in the first outer shell (for the 100 nm and 167 nm films) and in the first three outer shells (for the 57 nm film), respectively. As a consequence, the simulation model should remove about the same percentage of boundary voxels in the corresponding outer shells of ξ .

Some parts of the outer shells of B''' belong to thin branches of ZnO, therefore not the complete shells of ξ have to be removed. To include such thin branches into the model, we combine the model for the outer misspecifications introduced in Section 3.2.1 with the following algorithm to remove the boundary misspecifications.

For a given realization ξ , we iteratively remove those parts of the outer shells of ξ which are not connected to the set $\xi' \setminus \xi$ introduced in the previous section. In more detail, to correct the first outer shell, we first determine the set of all voxels $\eta \subset \xi$ belonging to the first outer shell. Subsequently, all voxels of the set $\eta_1 \subset \eta$ that are not touching the set $\xi' \setminus \xi$, that is, whose distance to $\xi' \setminus \xi$ is greater than 1, are removed. Now, the first outer shell is corrected. Those parts $\eta_2 = \eta \setminus \eta_1$ of the first outer shell that have not been removed since they were located near an outer misspecification are—for technical reasons—added to the set $\xi' \setminus \xi$ of simulated outer misspecifications. Hence, when correcting the second outer shell, the voxels near the set $(\xi' \setminus \xi) \cup \eta_2$ are not removed. This reproduces the thin branches as observed in the binarized ET data. To correct the third shell, the same procedure is repeated. The result after additionally adding the boundary misspecifications into the model is denoted by ξ'' .

3.2.3. *Interior misspecifications.* As mentioned in Section 2.3, the remaining misspecified voxels in B''' are classified as interior misspecifications. These interior misspecifications typically form small polymeric holes inside the ZnO domains.

Our modeling approach for the interior misspecifications is based on the assumption that the polymeric holes in the ZnO domains possess spherical shapes and are not overlapping, that is, we consider them as hard spheres.

Similarly to the modeling of the outer misspecifications, we assume that the centers of gravity of the interior misspecification clusters form a doubly stochastic point process, where again the cluster sizes are considered as marks. We assume the points of this point process to have a certain minimum distance r_h to each other because the interior misspecifications are seen as nonoverlapping spheres. In particular, given the realization ξ'' , that is, a realization of the marked point process for the macro-scale component of the ZnO phase introduced in Section 3.1 with included outer and boundary misspecifications as described in Sections 3.2.1 and 3.2.2, the centers of gravity of interior misspecification clusters are assumed to form a (conditional) Matérn hard-core process in $\xi \cap \xi''$. We assume that the marks of this point process are spheres with a constant radius $r = \frac{r_h}{2}$, that is, the interior misspecifications are modeled by nonoverlapping spheres with equal radii.

The Matérn hard-core process in \mathbb{R}^3 with intensity λ_h and hard-core radius r_h is a thinned homogeneous Poisson point process, where the remaining points have a distance of at least r_h to each other. Further details can be found, for example, in Illian et al. (2008). Given the set $\xi \cap \xi''$, the centers of gravity of interior misspecifications are then modeled by those points of the Matérn hard-core process which belong to $\xi \cap \xi''$. Hence, this model for the interior misspecifications can be called a doubly stochastic Matérn hard-core process.

To fit this model to real data, we first estimate the mean volume \bar{V} of the clusters for all three film thicknesses and transform this (mean) volume into a radius \hat{r} of a ball with the same volume \bar{V} . The corresponding radii obtained for the three considered data sets can be seen in Table 5. The hard-core radius \hat{r}_h of the Matérn hard-core process is then computed as $\hat{r}_h = 2\hat{r}$, which ensures that the spheres of radius \hat{r} centered at the points of the doubly stochastic Matérn hard-core process are not overlapping. For the intensity λ_h of the Matérn hard-core process we

TABLE 5
Estimated parameters for interior misspecifications

Parameter	57 nm film	100 nm film	167 nm film
Radius r	2.50	1.30	1.07
Intensity λ_h	1.37E-3	5.17E-3	5.12E-3

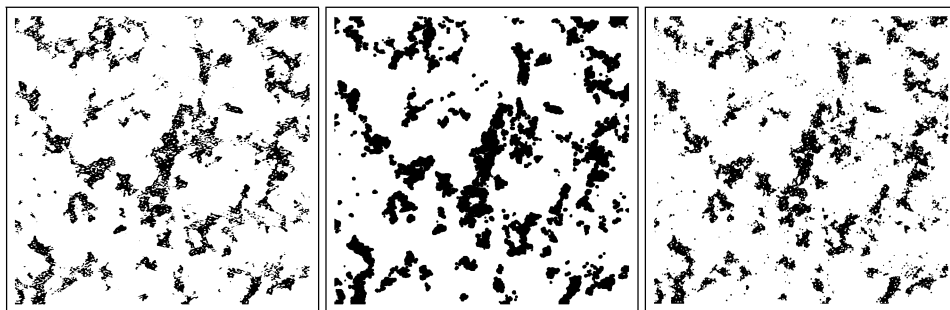


FIG. 12. *Left: 2D slice of 57 nm film, center: corresponding representation by a union of spheres, right: simulated correction using the model for the misspecified voxels applied to the representation by a union of spheres.*

consider the following natural estimator,

$$\hat{\lambda}_h = \frac{\text{number of disjoint clusters of interior misspecifications}}{|B'' \ominus b(o, r)|},$$

where $|B'' \ominus b(o, r)|$ denotes the volume of the set $B'' \ominus b(o, r)$. The values of $\hat{\lambda}_h$ obtained for the three data sets are shown in Table 5. From the results given in Table 5 it can be seen that, also with respect to interior misspecifications, the 57 nm film behaves rather different than the 100 nm, and 167 nm films: in the first case, there are fewer, but larger clusters of interior misspecifications than in the latter case. In the following, by ξ''' we denote a realization of our simulation model after including all three types of misspecifications.

Figure 12 shows a realization of the model for the micro-structure, where the micro-structure model is applied to the real data, more precisely, the representation by a union of spheres B''' of the 57 nm film. The two images on the left and the right sides of Figure 12 possess a high degree of visual resemblance. See also Section 4 for a more formal approach to model validation.

4. Model validation. To evaluate the goodness of fit, we compare model characteristics which have been computed from real and simulated data, respectively. On the one hand, we consider structural characteristics of the ZnO nanomorphology like the volume fraction of ZnO, the volume fraction of ZnO contributing to monotonous percolation pathways, and the distribution of spherical contact distances from polymer to ZnO. On the other hand, we consider a physical characteristic, the so-called exciton quenching probability. This characteristic describes the probability that a photo-excited particle generates charges. These characteristics have also been used in Oosterhout et al. (2009) to characterize the morphology of a photoactive layer, since they are closely related to the performance of solar cells. To compare the values of these characteristics, obtained from simulated and real data, we binarize the ET images using two extreme global thresholds as suggested

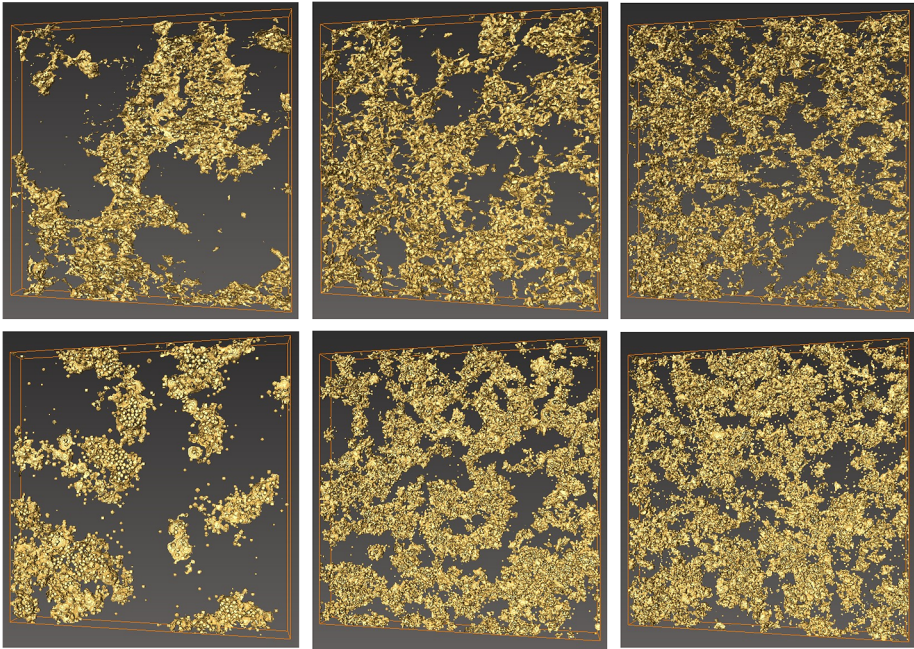


FIG. 13. 3D cutouts ($400 \times 400 \times 37$ voxels) of binarized ET images obtained by adaptive thresholding (1st row) and realizations of the complete model (2nd row); left: 57 nm film, center: 100 nm film, right: 167 nm film.

in Oosterhout et al. (2009). Recall that the two global thresholds have been chosen in such a way that the ZnO phase can be assumed to be a subset of the union of foreground voxels (high threshold) and, vice versa, the polymer phase is contained in the union of background voxels (low threshold).

It turns out that the estimated values obtained for most of the considered image characteristics of these two binarizations can be seen as lower and upper bounds, respectively, for corresponding values obtained for simulated images. In addition to this, we mention that, in accordance with the visual resemblance of images obtained from real and simulated data for the macro-scale component (see Figure 10) and the micro-scale component (see Figure 12) of the ZnO nanomorphology, the optical resemblance between binarized ET images obtained by adaptive thresholding and realizations of the complete simulation model is also quite well; see Figure 13.

4.1. *Checking morphological characteristics.* For a quantitative validation of the stochastic simulation model, we first consider structural characteristics of the ZnO nanomorphology. For this purpose, we generate 100 realizations of our model, estimate the considered characteristics for each of these realizations and compute their mean values. In the case of the spherical contact distance distribution function, the pointwise means are considered.

TABLE 6
Volume fractions of ZnO for globally thresholded and simulated images

		Volume fraction of ZnO	Volume fraction with connection	Volume fraction with monotonous connection
57 nm	Low threshold	0.098	0.934	0.872
	Simulated data	0.112	0.905	0.864
	High threshold	0.172	0.974	0.947
100 nm	Low threshold	0.133	0.890	0.673
	Simulated data	0.215	0.971	0.910
	High threshold	0.295	0.991	0.936
167 nm	Low threshold	0.128	0.851	0.630
	Simulated data	0.210	0.943	0.806
	High threshold	0.293	0.979	0.907

First, the volume fraction of ZnO is considered, which is one of the most important characteristics in structural modeling. The results given in Table 6 show that for all three film thicknesses, the volume fractions of ZnO computed from simulated data are between the corresponding bounds obtained from the globally thresholded ET images.

In the next step, the connectivity of the ZnO phase is considered. This also is an important characteristic, because only if there is a high connectivity, that is, if many percolation pathways exist, the produced charges can be transported to the electrodes, where current can be gripped. For estimating the connected and monotonously connected volume fractions of ZnO we applied the same methods as in Oosterhout et al. (2009). However, in general, the (conditional) connected and monotonously connected volume fractions of the foreground phase in globally thresholded images do not monotonously depend on the values of global thresholds. But as shown in Figure 14, this is the case for the globally thresholded ET data of photoactive layers of polymer-ZnO solar cells. Hence, also with respect to connected volume fractions, the values for the two extreme thresholds can be seen as upper and lower bounds. With the exception of the 57 nm film, the values for the connected volume fractions computed from simulated data, given in Table 6, are nicely between the corresponding values obtained from globally thresholded ET images. Also, the relative errors between the values obtained for the adaptively thresholded ET images and simulated images are rather small; see Table 7.

Finally, the spherical contact distribution function $F^{SCD} : [0, \infty) \rightarrow [0, 1]$ of the ZnO phase is considered, where $F^{SCD}(t)$ can be interpreted as a conditional probability that the minimum distance from a randomly chosen location to the ZnO phase is smaller or equal than $t \geq 0$, provided that the considered location belongs to the polymer phase.

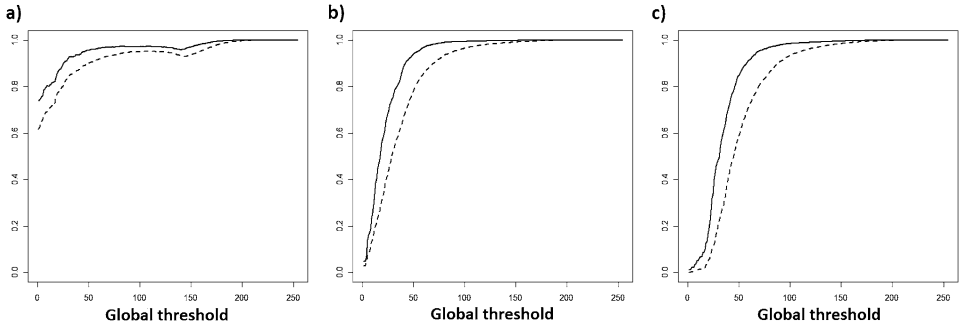


FIG. 14. Volume fractions of connected (solid lines) and monotonously connected (dashed lines) foreground phase, in dependence of the global threshold; a = 57 nm, b = 100 nm, c = 167 nm.

Similarly to the situation which we observed for the connected volume fractions considered above, it turns out that the spherical contact distribution functions of the foreground phase in globally thresholded ET images depend monotonously on the value of the global threshold. Hence, the estimated contact distribution functions \hat{F}_l^{SCD} and \hat{F}_u^{SCD} obtained for the two extreme thresholds can be seen as upper and lower bounds, respectively; see Figure 15. In addition to this, the spherical contact distribution \hat{F}^{SCD} obtained from simulated data is shown in Figure 15, where $\hat{F}_l^{SCD}(t) \leq \hat{F}^{SCD}(t) \leq \hat{F}_u^{SCD}(t)$ for all considered $t \geq 0$ and for all three layer thicknesses.

In summary, we can conclude that our model fits very well to real data regarding the considered structural characteristics. As the model has been developed for analyzing the influence of morphology on the performance of solar cells, we also

TABLE 7
Volume fractions of ZnO for adaptively thresholded and simulated images

		Volume fraction of ZnO	Volume fraction with connection	Volume fraction with monotonous connection
57 nm	Adaptive threshold	0.133	0.963	0.928
	Simulated data	0.112	0.905	0.864
	Relative error	-0.158	-0.060	-0.069
100 nm	Adaptive threshold	0.211	0.980	0.888
	Simulated data	0.215	0.971	0.910
	Relative error	0.019	-0.009	0.025
167 nm	Adaptive threshold	0.209	0.970	0.851
	Simulated data	0.210	0.943	0.806
	Relative error	0.005	-0.028	-0.053

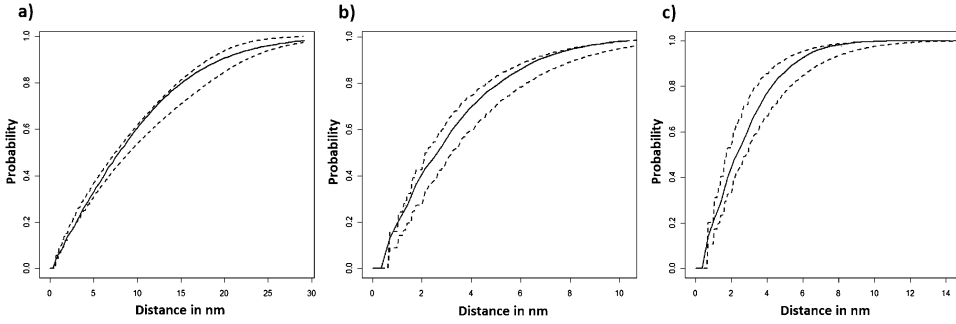


FIG. 15. Spherical contact distribution functions. The lower and upper bounds \widehat{F}_l^{SCD} and \widehat{F}_u^{SCD} obtained from globally thresholded ET images are plotted as dashed lines, the corresponding results from simulated image data as solid lines; $a = 57$ nm, $b = 100$ nm, $c = 167$ nm.

consider a physical characteristic for model validation which is described in the following section.

4.2. *Checking probabilities of exciton quenching.* Quenching efficiency η_Q is the probability of a random exciton being quenched; see Section 2.1. It is an elementary but important physical characteristic for the efficiency of solar cells.

In a hybrid polymer-ZnO solar cell, absorption of light by the polymer phase does not directly yield free charge carriers. Instead excitons are formed. It is only at the interface of the polymer and ZnO phase that free charges are generated by quenching (splitting) of excitons. It is therefore of the utmost importance that excitons are able to reach this interface. The exciton diffusion length in conjugated polymers is typically a few nanometers, which puts a considerable constraint on the morphology of polymer solar cells. In other words, the efficiency of exciton quenching is very sensitive to morphology, making it a suitable way to validate our model.

Suppose that the polymer phase $B^c = W \setminus B$ is given in a cubic sampling window $W \subset \mathbb{R}^3$. Then, the overall efficiency η_Q of exciton quenching can be obtained from the field $\{n(x), x \in B^c\}$ of local exciton densities in the polymer phase. The exciton density field $\{n(x), x \in B^c\}$ can be computed by solving the steady-state diffusion equation [see Oosterhout et al. (2009)]

$$0 = \frac{dn(x)}{dt} = -\frac{n(x)}{\tau} + D\nabla^2 n(x) + g, \quad x \in B^c,$$

where D is the diffusion constant, τ is the exciton life time, and g is the rate of exciton generation. As a boundary condition we require that all excitons at the polymer-ZnO interface be quenched, that is, $n(x) = 0$ for all $x \in \partial B^c \setminus \partial W$. For $x \in \partial B^c \cap \partial W$, cyclic boundary conditions are applied in all directions. The exciton lifetime and exciton diffusion rate in P3HT are taken from the literature: $\tau = 400$ ps and $D = 1.8 \cdot 10^{-7}$ m² s⁻¹; see Shaw, Ruseckas and Samuel (2008).

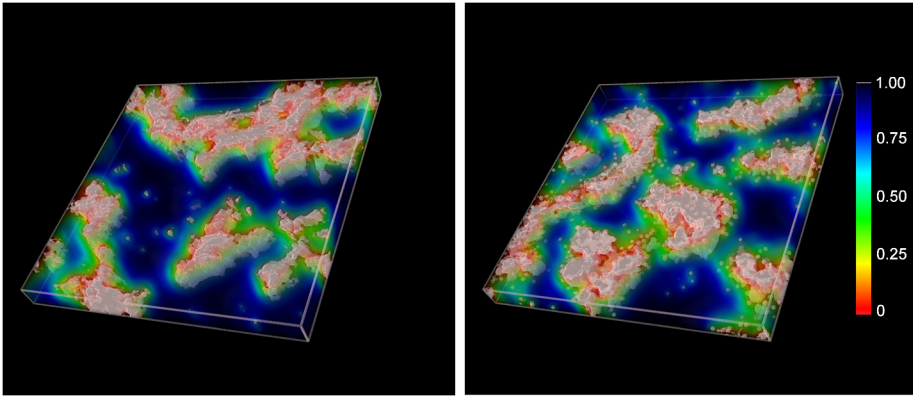


FIG. 16. The local exciton density $n(x)$ normalized to τg for adaptively thresholded ET (left) and simulated (right) data. The scalebar, specifying the density of excitons, applies to both images.

The rate of exciton generation g is just a scaling factor, where we use a value of $g = 10^{27} \text{ m}^{-3} \text{ s}^{-1}$ which is typical for 1-sun conditions.

The diffusion equation is solved numerically to a relative error of less than 10^{-3} . Figure 16 shows local exciton density fields $\{n(x), x \in B^c\}$ for adaptively thresholded and simulated data, respectively.

Once $\{n(x), x \in B^c\}$ is known, the quenching efficiency η_Q follows from $\eta_Q = 1 - \bar{n}/(\tau g)$, where \bar{n} is the average exciton density in the polymer domain B^c . Figure 17 compares the quenching efficiencies for original and simulated data. The quenching efficiency is also monotonously depending on the global threshold. Hence, the values of η_Q obtained for the two extreme thresholds can be seen as lower and upper bounds. The values of the quenching efficiency for the simulated data lie well within these lower and upper bounds; see Figure 17. The small relative errors displayed in Table 8 show that our model fits very well to real data, where quenching efficiencies of adaptively thresholded ET images are compared with those of simulated data.

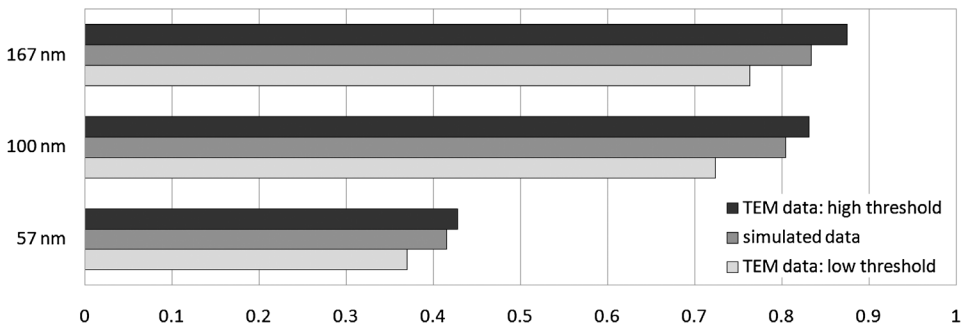


FIG. 17. Quenching efficiencies for globally thresholded and simulated images.

TABLE 8
Quenching efficiencies for adaptively thresholded and simulated images

	57 nm film	100 nm film	167 nm film
Adaptive threshold	0.418	0.794	0.819
Simulated data	0.416	0.805	0.834
Relative error	-0.010	0.014	0.018

5. Conclusions and outlook. In the present paper we developed a parameterized stochastic simulation model for the nanostructure of photoactive layers of hybrid polymer-ZnO solar cells. The model is based on tools from stochastic geometry. Additional to the model itself, we developed a method to fit its parameters to real 3D ET image data.

To establish our model, the adaptively thresholded ET images are segmented using a stochastic algorithm which consists of two main steps. First, the images are morphologically smoothed in order to slightly decrease their structural complexity. Then, the morphologically smoothed binary images are represented by a system of overlapping spheres, which can be interpreted as a realization of a 3D marked point process, where the sphere centers are the locations of points and the corresponding radii are their marks. For the stochastic simulation model, we use a correlated vector of 2D elliptical Matérn cluster processes, where the points are subsequently marked to create a 3D marked point process. To complete the model, that is, to include the structural details which were omitted due to the morphological smoothing, a stochastic simulation model for this “micro-scale” component is developed afterward.

As our stochastic simulation model is fully parameterized, we also developed techniques for the estimation of the model parameters of all model components. Thus, we are able to fit the simulation model to the ET image data described in Section 2.2.

Finally, we validated the simulation model by comparing structural and physical characteristics computed from simulated image data with the corresponding characteristics obtained from globally and adaptively thresholded ET images, respectively. In particular, the quenching efficiencies computed for realizations of the simulation model agree very well with those of the ET images. Hence, our model nicely reflects the diffusion of excitons.

Since we were able to fit our model to 3D ET data, it has already proved its capability to represent realistic nanostructures of photoactive layers of hybrid polymer-ZnO solar cells. The fact that the model is parameter-based enables us to predict morphologies for film thicknesses, which have not (yet) been imaged by 3D ET, by interpolating or extrapolating the fitted model parameters. Due to a strong correlation between morphology and efficiency of polymer solar cells [see Oosterhout

et al. (2009)], the developed simulation model is of significant importance for further investigations of polymer solar cells. In a forthcoming paper we will also investigate the transport processes of charges to the electrodes as described in Koster (2010), additional to the structural and physical characteristics considered in the present paper. By generating virtual morphologies, which are generated as realizations of the developed model with different parameter configurations, and investigating the transport processes of electrons and excitons therein, the spatial stochastic model will be used to identify morphologies of improved efficiency with respect to the considered physical characteristics.

We also remark that the modeling approach developed in the present paper can be applied to various other kinds of image data, including geographical data considered, for example, in ecology. Then, for instance, the Markov chain of Matérn cluster processes introduced in Section 3.1.2 may be viewed as a sequence of dependent 2D point processes through time, which can model, for example, the temporal movements of species in a given region.

Acknowledgments. The authors would like to thank Image Analysis & Stereology for permission to reprint Figures 1–3 taken from Thiedmann et al. (2011). Part of this work was done while Volker Schmidt was visiting the Isaac Newton Institute for Mathematical Sciences, Cambridge.

REFERENCES

- BADDELEY, A. J., HOWARD, C. V., BOYDE, A. and REID, S. (1987). Three-dimensional analysis of the spatial distribution of particles using the tandem-scanning reflected light microscope. *Acta Stereologica* **6** 87–100.
- BADDELEY, A. J., GREGORI, P., MATEU, J., STOICA, R. and STOYAN, D., EDS. (2006). *Case Studies in Spatial Point Process Modeling. Lecture Notes in Statist.* **185**. Springer, New York. MR2229141
- BALLANI, F., DALEY, D. J. and STOYAN, D. (2005). Modelling the microstructure of concrete with spherical grains. *Computational Materials Science* **35** 399–407.
- BEIL, M., FLEISCHER, F., PASCHKE, S. and SCHMIDT, V. (2005). Statistical analysis of the three-dimensional structure of centromeric heterochromatin in interphase nuclei. *J. Microsc.* **217** 60–68. MR2109400
- BLAYVAS, I., BRUCKSTEIN, A. and KIMMEL, R. (2006). Efficient computation of adaptive threshold surfaces for image binarization. *Pattern Recognition* **39** 89–101.
- BRABEC, C., SCHERF, U. and DYAKONOV, V. (2008). *Organic Photovoltaics: Materials, Device Physics, and Manufacturing Technologies*. Wiley-VCH, Weinheim.
- DALEY, D. J. and VERE-JONES, D. (2008). *An Introduction to the Theory of Point Processes. Vol. II: General Theory and Structure*, 2nd ed. Springer, New York. MR2371524
- DIGGLE, P. J. (2003). *Statistical Analysis of Spatial Point Patterns*, 2nd ed. Arnold, London.
- GELFAND, A. E., DIGGLE, P. J., FUENTES, M. and GUTTORP, P. (2010). *Handbook of Spatial Statistics*. CRC Press, Boca Raton, FL. MR2761512
- ILLIAN, J., PENTTINEN, A., STOYAN, H. and STOYAN, D. (2008). *Statistical Analysis and Modelling of Spatial Point Patterns*. Wiley, Chichester. MR2384630
- KENDALL, W. S. and MOLCHANOV, I., EDS. (2010). *New Perspectives in Stochastic Geometry*. Oxford Univ. Press, Oxford. MR2668353

- KOSTER, L. J. A. (2010). Charge carrier mobility in disordered organic blends for photovoltaics. *Phys. Rev. B* **81** 205318.
- MØLLER, J. and WAAGEPETERSEN, R. P. (2004). *Statistical Inference and Simulation for Spatial Point Processes. Monogr. Statist. Appl. Probab.* **100**. Chapman & Hall/CRC, Boca Raton, FL. MR2004226
- OHSER, J. and MÜCKLICH, F. (2000). *Statistical Analysis of Microstructures in Materials Science*. Wiley, New York.
- OOSTERHOUT, S. D., WIENK, M. M., VAN BAVEL, S. S., THIEDMANN, R., KOSTER, L. J. A., GILOT, J., LOOS, J., SCHMIDT, V. and JANSSEN, R. A. J. (2009). The effect of three-dimensional morphology on the efficiency of hybrid polymer solar cells. *Nature Materials* **8** 818–824.
- SHAW, P. E., RUSECKAS, A. and SAMUEL, I. D. W. (2008). Exciton diffusion measurements in poly(3-hexylthiophene). *Advanced Materials* **20** 3516–3520.
- STOICA, R. S., GREGORI, P. and MATEU, J. (2005). Simulated annealing and object point processes: Tools for analysis of spatial patterns. *Stochastic Process. Appl.* **115** 1860–1882. MR2172890
- STOYAN, D., KENDALL, W. S. and MECKE, J. (1995). *Stochastic Geometry and Its Applications*, 2nd ed. Wiley, Chichester.
- THIEDMANN, R., HASSFELD, H., STENZEL, O., KOSTER, L. J. A., OOSTERHOUT, S. D., VAN BAVEL, S. S., WIENK, M. M., LOOS, J., JANSSEN, R. A. J. and SCHMIDT, V. (2011). A multi-scale approach to the representation of 3D images, with application to polymer solar cells. *Image Anal. Stereol.* **30** 19–30.
- VAN BAVEL, S. S., SOURTY, E., DE WITH, G. and LOOS, J. (2009). Three-dimensional nanoscale organization of bulk heterojunction polymer solar cells. *Nano Lett.* **9** 507–513.
- YANG, X. and LOOS, J. (2007). Toward high-performance polymer solar cells: The importance of morphology control. *Macromolecules* **40** 1353–1362.
- YANOWITZ, S. D. and BRUCKSTEIN, A. M. (1989). A new method for image segmentation. *Computer Vision, Graphics, and Image Processing* **46** 82–95.

O. STENZEL
 H. HASSFELD
 R. THIEDMANN
 V. SCHMIDT
 INSTITUTE OF STOCHASTICS
 ULM UNIVERSITY
 89069 ULM
 GERMANY
 E-MAIL: ole.stenzel@uni-ulm.de
 henrik.hassfeld@uni-ulm.de
 ralf.thiedmann@uni-ulm.de
 volker.schmidt@uni-ulm.de

L. J. A. KOSTER
 S. D. OOSTERHOUT
 S. S. VAN BAVEL
 M. M. WIENK
 J. LOOS
 R. A. J. JANSSEN
 CHEMICAL ENGINEERING AND CHEMISTRY
 MOLECULAR MATERIALS AND NANOSYSTEMS
 EINDHOVEN UNIVERSITY OF TECHNOLOGY
 5600 MB EINDHOVEN
 THE NETHERLANDS
 E-MAIL: l.j.a.koster@tue.nl
 s.d.oosterhout@tue.nl
 s.s.v.bavel@tue.nl
 m.m.wienk@tue.nl
 j.loos@tue.nl
 r.a.j.janssen@tue.nl